Chemical Science

EDGE ARTICLE

View Article Online
View Journal | View Issue

Cite this: *Chem. Sci.*, 2018, **9**, 1221

Exchange coupling and single molecule magnetism in redox-active tetraoxolene-bridged dilanthanide complexes†

Peng Zhang,[a] Mauro Perfetti,[ab] Michal Kern,[a] Philipp P. Hallmen,[a] Liviu Ungur,[c] Samuel Lenz,[a] Mark R. Ringenberg,[d] Wolfgang Frey,[e] Hermann Stoll,[f] Guntram Rauhut[f] and Joris van Slageren[*a]

Received 13th November 2017
Accepted 7th December 2017

DOI: 10.1039/c7sc04873d

rsc.li/chemical-science

Tetraoxolene radical-bridged lanthanide SMM systems were prepared for the first time by reduction of the respective neutral compounds. Magnetic measurements reveal the profound influence of the radical center on magnetic behavior. Strong magnetic couplings are revealed in the radical species, which switch on SMM behavior under zero applied field for Dy^{III} and Tb^{III} compounds. HFEPR spectra unravel the contributions of the magnetic coupling and the magnetic anisotropy. For Gd^{III} this results in much more accurate magnetic coupling parameters with respect to bulk magnetic measurements.

Introduction

Tetraoxolene ligands and its derivatives, where one or more of the oxygens are replaced by nitrogen with an appropriate R-group, have been extensively used as bridges in the assembly of transition metal complexes showing peculiar magnetic and/or conducting properties.[1–3] One major reason is their fascinating electronic structures arising from the redox–rich properties, and extensive tuning of chemical and physical properties is available as a result.[4,5] In particular, upon either oxidation or reduction, these ligands can form a delocalized π radical system, which can lead to strong exchange couplings with paramagnetic ions and can efficiently transmit electronic effects between the bridged metal centers, as revealed in a number of transition metal dimers.[6–8] Nevertheless, tetraoxolene-based, radical-bridged systems have not been reported in lanthanide chemistry. To date, only mono-semiquinonato lanthanide systems were presented,[9,10] as well as tetraoxolene-bridged lanthanide dimers with closed-shell bridges.[11,12] Significantly, a strong antiferromagnetic coupling of over 10 cm^{-1} was achieved in a gadolinium–semiquinone complex,[13,14] whilst the experimental and DFT investigations of the Y^{III} analogue revealed significant spin delocalization of the oxygen toward the yttrium site,[15] suggesting the strong ability of dioxolene and, by extension, tetraoxolene radicals to mediate magnetic exchange couplings between lanthanide ions. Therefore, tetraoxolene radical bridges are quite promising for achieving strong magnetic coupling in polynuclear lanthanide-based system with the aim of improving single molecule magnet (SMM) properties.

In fact, the development of exchange coupled polynuclear lanthanide clusters with radical bridges is seen as one of the most efficient routes to a high-performance SMM since the discovery of N_2^{3-}-radical-bridged lanthanide SMM showing many times less efficient tunneling than in single ion systems.[16–18] Nevertheless, different from the common lanthanide SMMs, experiencing an unparalleled growth recently,[19,20] synthetic difficulty leads to slow progress in radical bridge-containing systems with only a few successful examples, such as $N_2^{3-\bullet}$, $bpym^{-\bullet}$, $tppz^{-\bullet/3-\bullet}$, $bptz^{-\bullet}$, $ind^{3-\bullet}$, $HAN^{3-\bullet}$.[17,18,21–25] All these bridging ligands are nitrogen-based. Here we synthesized a family of tetraoxolene bridged lanthanide dimers, $[(HBpz_3)_2Ln(\mu\text{-}CA)Ln(HBpz_3)_2]\cdot 2CH_2Cl_2$ (**1Ln**, Ln = Dy, Tb, Gd, Y, $HBpz_3^-$ = hydrotris(pyrazol-1-yl)borate, CA^{2-} = chloroanilate). Chemical reduction by cobaltocene leads to the isolation of radical bridged species, $[(HBpz_3)_2Ln(\mu\text{-}CA^{\bullet})Ln(HBpz_3)_2]^-\cdot[CoCp_2]^+$ (**2Ln**, Ln = Dy, Tb, Gd, Y). Magnetic measurements reveal strong magnetic coupling between the radical and the lanthanide ions (J = 4.17 cm^{-1} for **2Gd**), promoting the appearance of SMM behavior in zero applied field for **2Dy** and

[a]*Institut für Physikalische Chemie, Universität Stuttgart, Pfaffenwaldring 55, D-70569, Stuttgart, Germany. E-mail: slageren@ipc.uni-stuttgart.de*

[b]*Department of Chemistry, University of Copenhagen, Universitetparken 5, 2100 Copenhagen, Denmark*

[c]*Theory of Nanomaterials Group, INPAC-Institute of Nanoscale Physics and Chemistry, Katholieke Universiteit Leuven, 3001 Leuven, Belgium*

[d]*Institut für Anorganische Chemie, Universität Stuttgart, Pfaffenwaldring 55, D-70569 Stuttgart, Germany*

[e]*Institut für Organische Chemie, Universität Stuttgart, Pfaffenwaldring 55, D-70569 Stuttgart, Germany*

[f]*Institut für Theoretische Chemie, Universität Stuttgart, Pfaffenwaldring 55, D-70569 Stuttgart, Germany*

† Electronic supplementary information (ESI) available: Experimental procedures, crystallography, magnetic properties measurements, and *ab initio* details. CCDC 1568172–1568175. For ESI and crystallographic data in CIF or other electronic format see DOI: 10.1039/c7sc04873d

2Tb. Furthermore, the magnetic coupling in **1Gd** and **2Gd** was studied by means of high-frequency electron paramagnetic resonance (HFEPR) spectroscopy, which gives more accurate information on the magnetism than magnetic measurements.

Results and discussion

Syntheses, structures, and electrochemistry

The non-radical bridged lanthanide dimers **1Ln** were synthesized from an aqueous solution of H_2CA, $K(HBpz_3)$ and $LnCl_3 \cdot xH_2O$ in a 1 : 4 : 2 stoichiometric ratio. The recrystallization of the crude products in dichloromethane–acetonitrile solution afforded single crystals suitable for X-ray analysis. Compounds **1Ln** are isostructural, and crystallize in monoclinic space group $P2_1/n$ (Table S1†). This structure has been previously reported for **1Dy** and **1Y**.[11] The molecular structure of **1Dy** is shown in Fig. 1, where two eight-coordinate Dy ions are related by a crystallographic inversion center and each is surrounded by a distorted square-antiprismatic environment (SAP). Furthermore, the conjugated CA^{2-} ligand connects two Dy centers with a Dy–Dy distance of 8.64(9) Å, which is much longer than in the oxalate-bridged Dy_2 compound reported in 2010.[26] Therefore, the magnetic interaction is expected to be very weak in these compounds. The CA^{2-} bridge has the advantage over oxalate in being (electro)chemically reducible in a facile manner, as seen in Scheme 1. The generation of a radical species is expected to enhance the magnetic exchange coupling between lanthanide ions despite the large separation.

To investigate their redox properties, electrochemical measurements were carried out. Cyclic voltammograms reveal that all compounds display two one-electron reduction steps (Fig. 2 and S1†) related to CA^{2-} bridge in CH_2Cl_2/0.1 M Bu_4NPF_6 with the parameters shown in Table 1. Significantly, a reversible reduction is observed near −1.05 V *vs.* Fc/Fc^+, and the peak current ratios close to 1 reveal the electrochemical stability of the $CA^{3-\bullet}$-radical species formed upon reduction. Furthermore, the first reduction process is reversible in different solvents (Fig. S2†), which is promising for isolation of the chemically reduced species. The UV/vis spectrum of **1Ln** displays a strong absorption band in the near UV, which is also seen at shorter wavelengths in the H_2CA ligand (Fig. S3†). UV/vis spectroelectrochemical measurements reveal the decrease of this band upon reduction and the concurrent appearance of a new band between 430 and 490 nm, which we attribute to a radical-based π–π* transition.

Encouraged by these results, we attempted the chemical reduction of all compounds employing cobaltocene ($CoCp_2$/$CoCp_2^+$, $E_{1/2} = -1.33$ V) as reducing agent. The treatment with cobaltocene ($CoCp_2$) leads to precipitation of the desired

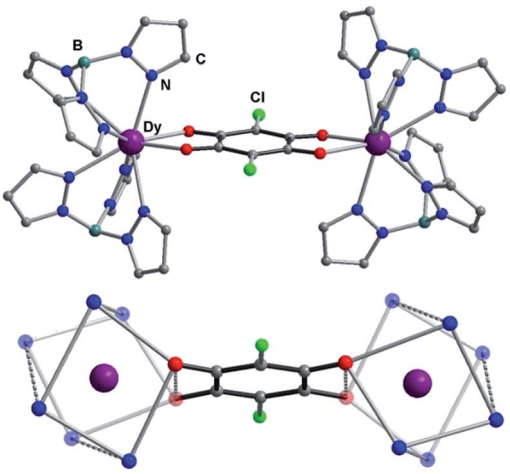

Fig. 1 (Top) Crystal structure of compounds with lattice solvent molecules and hydrogen atoms omitted for clarity. Colour code: Dy purple, O red, N blue, C grey, Cl blue. (Bottom) Depiction of molecular structure, omitting the noncoordinating atoms of the ancillary ligands, highlighting the coordination polyhedra around the lanthanide ions.

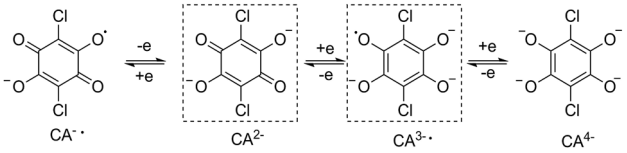

Scheme 1 Various redox forms of the bridging chloranilate. The forms in dashed box are used here.

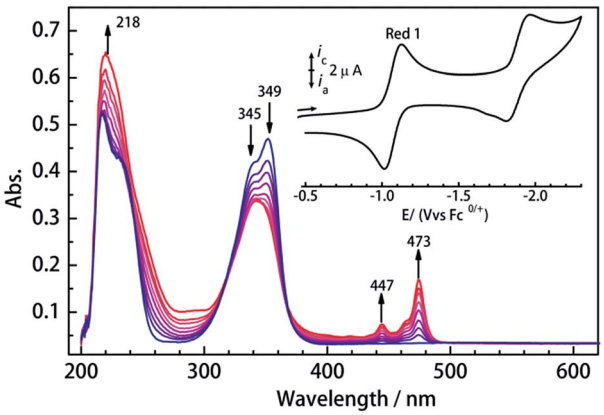

Fig. 2 Changes in the UV/Vis spectrum of **1Dy** during first reduction in CH_2Cl_2/0.1 M Bu_4NPF_6 of supporting electrolyte. Ag/Ag^+ reference, Pt mesh working, Pt counter electrode. (Insert, cyclic voltammogram of **1Dy** in CH_2Cl_2/0.1 M Bu_4NPF_6 measured at 295 K. $Fc^{0/+}$ = ferrocene/ferrocenium couple.).

Table 1 Redox potentials *versus* $Fc^{0/+}$ obtained from cyclic voltammetry experiments

	Red 1			Red 2	
	$E_{1/2}{}^a$/V	E_{pc}/V	i_{pa}/i_{pc}	E_{pc}/V	i_{pa}/i_{pc}
1Dy	−1.09	−1.15	0.957	−2.09	n.a.
1Tb	−1.07	−1.13	0.977	−1.94	n.a.
1Gd	−1.14	−1.21	0.938	−2.02	n.a.
1Y	−1.10	−1.25	0.964	−2.07	n.a.

[a] $E_{1/2}$ for reversible processes, in CH_2Cl_2/0.1 M Bu_4NPF_6 at 298 K glassy carbon working electrode, Pt counter electrode, Ag reference electrode.

species as green powders. The advantage of employing cobaltocene is that the resultant cation $[CoCp_2]^+$ is a diamagnetic species and silent to all the spectroscopic and magnetic measurements discussed hereafter.[27] Even though only low quality crystals could be obtained by recrystallization in acetonitrile, the results from ESI-MS (Fig. S4–S8†), IR spectra (Fig. S9†) and elemental analysis confirm the clean formation of $[(HBpz_3)_2Ln(\mu\text{-}CA^{\bullet})Ln(HBpz_3)_2]^- \cdot [CoCp_2]^+$ (**2Ln**). Taking **2Dy** as an example, the ESI-MS (Fig. 3) under negative mode reveals a peak at $m/z = 1384$, corresponding to the molecular ion of the anion complex, which exhibits the same mass and splitting pattern as the non-radical compound **1Dy**. Furthermore, IR spectra of the reduced compounds (Fig. 4) are similar to those of the non-reduced compounds but with an additional strong absorption at ~1450 cm^{-1}, which is ascribed to the stretching vibration of –C–O$^{\bullet}$ radical.[2] In addition, the spectra show weak absorptions of $[CoCp_2]^+$ at 1022 and 828 cm^{-1}.[28]

Static magnetic susceptibility

Static magnetic measurements for all compounds were carried out in an applied field of 1000 Oe between 1.8 and 300 K with a Quantum-Design MPMS magnetometer (Fig. 5). The $\chi_M T$ values of complexes **1Dy**, **1Tb**, **1Gd** at room temperature are 29.5, 24.2, and 15.50 cm^3 K mol^{-1}, close to the theoretical values of 28.34, 23.64, and 15.76 cm^3 K mol^{-1} for two non-interacting Dy^{III}, Tb^{III}, and Gd^{III} ions, respectively. On decreasing the temperature to 1.8 K, the $\chi_M T$ values for **1Dy** and **1Tb** decrease, which we attribute to the depopulation of excited crystal field states. Similar results were recently obtained.[11] For **1Gd** no such

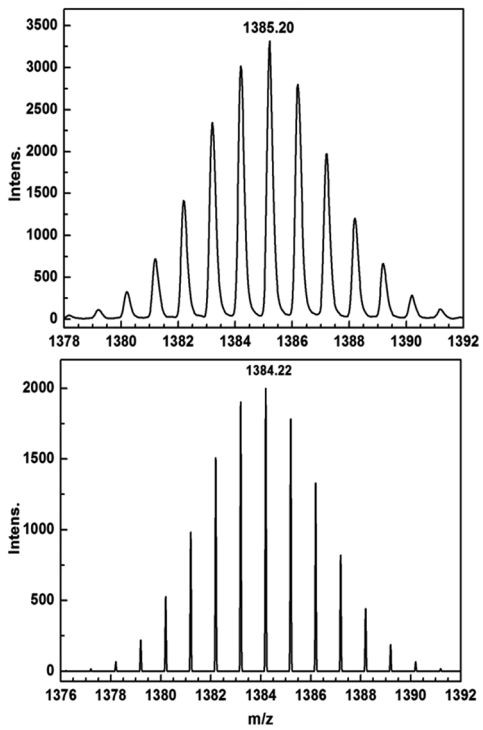

Fig. 3 ESI-MS spectra of **1Dy** (top) and **2Dy** (bottom) showing the isotope pattern of the molecular ion peaks at $m/z = 1385$ ($[M + H]^+$) and 1384 (M^-).

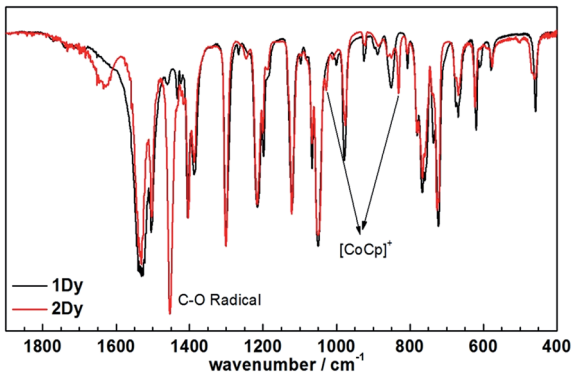

Fig. 4 The comparison between IR spectra of **1Dy** and **2Dy**.

decrease is observed in agreement with the essentially isotropic electronic ground state of Gd^{III}, and the absence of strong magnetic couplings in this compound. Starkly different static magnetic behavior is found for the reduced compounds **2Ln**. As shown in Fig. 5, the $\chi_M T$ values at room temperature are slightly higher than that in the corresponding non-reduced compounds due to the additional radical centre (Curie constant at room temperature: 0.375 cm^3 K mol^{-1}). Upon lowering the temperature, the $\chi_M T$ values decrease more rapidly than in the corresponding neutral complexes, reaching minimum values at 50 K and 20 K for **2Dy** and **2Tb** respectively. Remarkably, an increase of $\chi_M T$ is observed upon further lowering the temperature, clearly connected with strong magnetic interactions between lanthanide centers and the delocalized π radical. Below 6 K, **2Dy** exhibits a sudden decrease of the $\chi_M T$ value that indicate a possible magnetic blocking behavior, as observed for other radical bridged SMMs.[17,22] Given the large magnetic anisotropy arising from strong spin orbital interactions for Dy^{III} and Tb^{III} ions it is impossible to accurately quantify the magnetic coupling parameters from susceptibility data alone. The room temperature $\chi_M T$ value for **2Gd** is again slightly higher than that of the neutral complex **1Gd**, but in contrast, it decreases upon lowering the temperature before increasing again. The absence

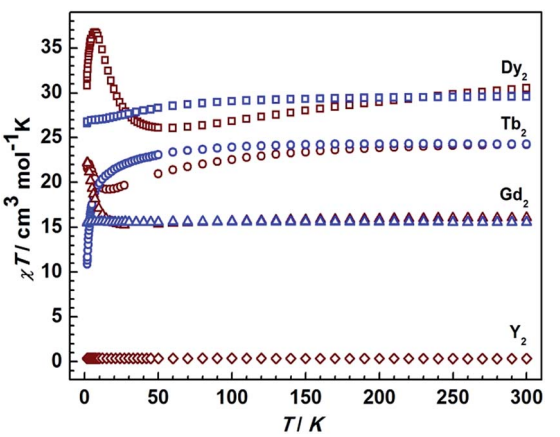

Fig. 5 Temperature dependence of the $\chi_M T$ values at 1000 Oe for compounds **1Ln** and **2Ln**. The blue and brown symbols correspond to neutral and radical compounds, respectively.

of first order orbital angular momentum for Gd compounds[29–31] allows employing a spin-only Hamiltonian $\mathscr{H} = J\hat{S}_{rad}(\hat{S}_{Gd1} + \hat{S}_{Gd2})$ to fit the data. A value of $J = 4.17$ cm^{-1} was obtained, revealing substantial antiferromagnetic coupling between the Gd^{III} centers and the radical bridge (Fig. S10†). The magnitude is smaller than in the case of the mono-semiquinonato system ($J = 11.4$ cm^{-1}),[13] and it is relatively small compared with the N-bearing radical bridged systems (12–54 cm^{-1}), which can possibly be ascribed to the less diffuse orbitals and stronger electronegativity of oxygen donor.[9] However, it is beneficial to stabilize such a radical species, and indeed the solid compounds exhibit the enhanced stability even upon exposure to the atmosphere. Finally, the temperature-independent $\chi_M T$ value of 0.35 cm^3 K mol^{-1} is consistent with the expected value of 0.375 cm^3 K mol^{-1} for **2Y**.

Magnetization data at fields of 0–70 kOe below 5 K (Fig. S11†) was also collected, and the comparison to non-reduced compounds reveals faster increase of magnetization at low field and lower high-field magnetization for radical-bridged species **2Ln**, which is completely consistent with the strong antiferromagnetic exchange between lanthanide and radical. The saturation magnetization of 12.7 μ_B reveals an $S = 13/2$ ground state in **2Gd**. The saturation value of **1Ln** and **2Ln** (Ln = Dy, Tb) is also consistent with the ground state essentially consisting of the largest m_J state (see *ab initio*).

Dynamic magnetic susceptibility

Given the fascinating relaxation behavior of magnetization in radical-bridged dilanthanide systems,[16–18] variable-frequency ac susceptibility measurements were performed at variable temperatures (Fig. 6 and S12†). As shown in Fig. 6a and d, slow relaxation of the magnetization was detected at 1.8 K in both **1Dy** and **2Dy** as strong frequency- and field-dependent peaks of the out-of-phase (χ'') susceptibility. Significantly, at zero dc field, only **2Dy** shows a χ'' peak, and no peak was detected in **1Dy** in the measured frequency range from 0.1 Hz to 1000 Hz. This is indicative of improved SMM properties as a result of strong magnetic couplings between the Dy and radical centers in **2Dy**. Furthermore, the application of a dc field leads to the second relaxation process occurring at lower frequency in both compounds. The fast relaxation process remains on the edge of the frequency window for compound **1Dy**, while two relaxation processes could be nicely resolved in **2Dy**. The fast relaxation process in **2Dy** is progressively quenched with increasing the field and disappears completely for fields stronger than 1000 Oe. Similar relaxation behavior was also observed in mononuclear [Dy(DOTA)],[32] a dinuclear, Cl-bridged cyclopentadienyldysprosium compound[33] and U(H$_2$BPz$_2$)$_3$,[34] but the relaxation mechanism is still unclear. Here, two series of relaxation times (τ) can be extracted by the sum of two modified Debye functions for **2Dy** (Fig. S13, S14 and Table S2†). More importantly, the field dependence of slow relaxation process is drastically different from that observed for compound **1Dy** especially below 2000 Oe, suggesting an important effect from radical coupling.

The ac susceptibility was also investigated as a function of temperature in compounds **1Dy** and **2Dy** under 0 and 1000 Oe (optimum) field (Fig. 6). In zero dc field the χ'' signals in **2Dy** show well-resolved relaxation peaks between 1.8 and 3.2 K (Fig. 6b), but only slightly shifted in temperature, characteristic of the quantum tunneling regime.[35] The tunneling relaxation time is extracted to be 0.97 ms (Fig. 6f).

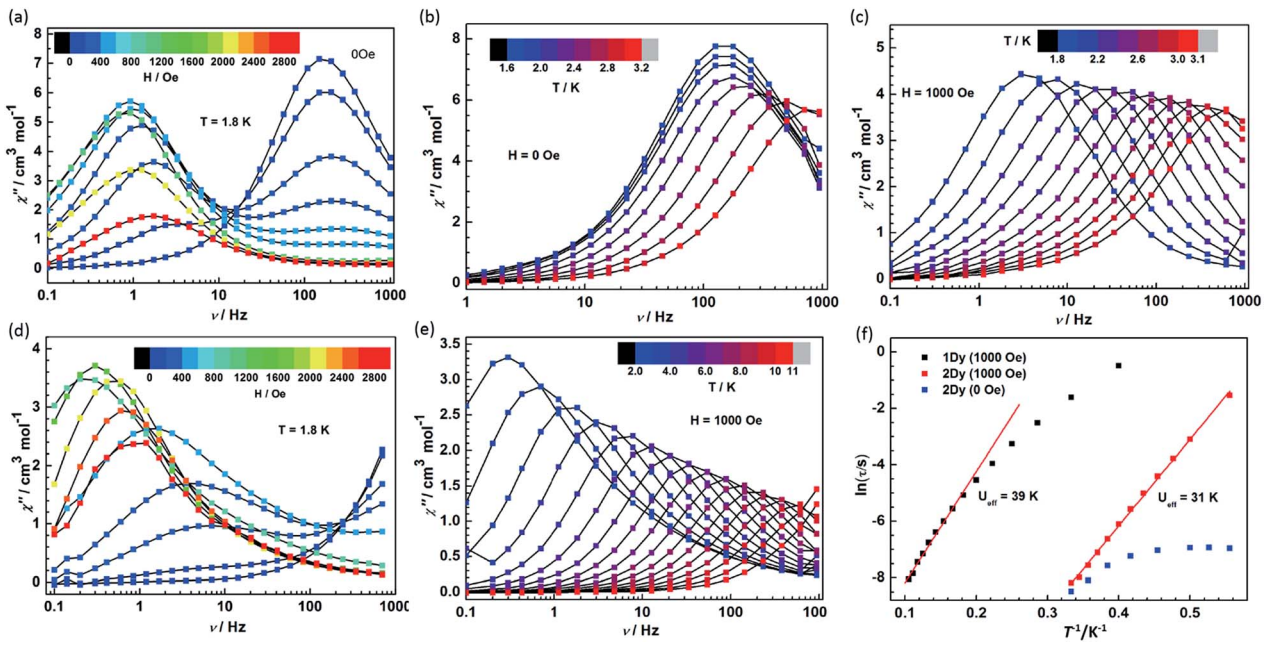

Fig. 6 (a) Field and frequency dependence of χ'' at 1.8 K for **2Dy**. (b) Temperature dependence of χ'' in zero dc field for **2Dy**. (c) Temperature dependence of χ'' in a 1000 Oe dc field for **2Dy**. (d) Field and frequency dependence of χ'' at 1.8 K for **1Dy**. (e) Temperature dependence of the χ'' susceptibility in a 1000 Oe external field for **1Dy**. (f) Plots of ln τ *versus* T^{-1} for **1Dy**, **2Dy** in 0 and 1000 Oe dc fields. The solid lines correspond to the Arrhenius fit.

In a dc field of 1000 Oe compounds **1Dy** and **2Dy** both show slow relaxation of magnetization, as indicated by the temperature-dependent χ'' peaks (Fig. 6c and e). The relaxation times can be extracted with a generalized Debye model, and an Arrhenius fit of temperature dependence gives their effective barriers (U_{eff}), 39 ± 2 and 31 ± 1 K, with $\tau_0 = 5.46 \times 10^{-6}$ and 7.33×10^{-9} s for **1Dy** and **2Dy**, respectively. A slightly different effective energy barrier value was reported for **1Dy**, due to the different frequency range employed there.[11] The relatively low values of the effective barriers already suggest that the Orbach relaxation pathway is not efficient for these systems in such temperature range, as commonly reported for Ln complexes.[36–38] In particular, the relaxation behavior persists in wider temperature range in compound **1Dy** but it exhibits a poor linear relationship in $\ln(\tau)$ *vs.* T^{-1} plots and uncommonly large τ_0 value (Fig. 6f). To explore the presence of other relaxation pathways we also tentatively fitted the temperature dependence of the relaxation times with an power (T^n) function obtaining $n = 5.6$ for **1Dy** and $n = 13.0$ for **2Dy** (Fig. S15†). These result clearly suggests that a Raman process could be responsible for the slow relaxation for **1Dy**, while the unphysically large exponent in **2Dy** indicates that the situation is more complicated, *e.g.* due to the participation of optical phonons/molecular vibrations.[16,39]

Furthermore, ac magnetic susceptibility data collected for **2Tb** also display out-of-phase susceptibility signals with a frequency and temperature dependence indicative of slow relaxation of magnetization (Fig. S16†). The effective barrier cannot be extracted given that only three data points available for which a maximum is observed. Even so it still reveals the large contribution of strong magnetic coupling on relaxation behaviour.

A careful comparison between the systems reported here and the Ln radical-bridged systems previously reported in literature can shed light on possible magnetochemical relations. The effective barrier obtained for **2Ln** is generally lower than the ones in $N_2^{3-\bullet}$, $bpym^{-\bullet}$ and $tppz^{-\bullet}$-bridged compounds. One key reason is the limitation of local coordination environment around lanthanide center, which leads to the weak crystal field splitting and large transverse anisotropy (*ab initio* calculations below), as indicated by the similar Dy^{III} SMMs with $HBpz_3^-$ ligands.[26,40,41] Recently an air stable tetrazine radical-bridged Dy^{III} SMM and its neutral counterpart by Dunbar *et al.* also exhibited the redox switching of magnetic relaxation dynamics.[23] In the same way the use of β-diketonate leads to a weak blocking behavior. The strong contrast to the radical systems with cyclopentadienyl ligand (Cp)[21,22,25] suggests that it is better to use Cp as ancillary ligands, which supports a stronger axial crystal field.

Remarkably, ac susceptibility measurements on **2Y** reveal a field-induced slow relaxation behavior of magnetization (Fig. 7), which is unexpected in light of the diamagnetic nature of the Y^{III} ion. Furthermore, in a dc field of 5000 Oe χ'' shows temperature-dependent relaxation peaks until 15 K (Fig. S17†). The relaxation times were extracted and an Arrhenius fit of the high temperature region gives unphysical parameters of $U_{eff} = 20$ K and $\tau_0 = 1.20 \times 10^{-4}$ s.[16] Here the in-phase component of the ac susceptibility decreases to close to zero at low temperatures. To have

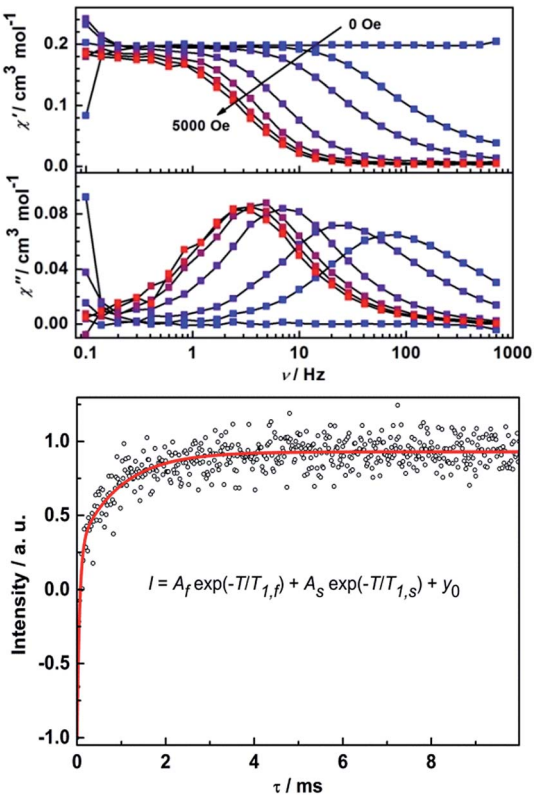

Fig. 7 Field and frequency dependence of the out-of-phase ac susceptibility at 1.8 K for **2Y**, and the inversion recovery experiment of 1 mM **2Y** in acetonitrile at 7 K, 35 GHz and 1249 mT fitted with equation (red line).

a quantitative idea of the fraction of the sample that relaxes slowly we can compare the dc susceptibility and the (χ_T–χ_S) value from ac measurements. It reveals more than 90% of the sample is slowly relaxing given the different applied dc field (Fig. S17†). This excludes the possibility of the relaxation arising from a magnetic impurity. To further characterize the observed slow relaxation, pulsed Q-band EPR was carried out on a frozen solution sample of **2Y** at 7 K.[42] The spin–lattice relaxation time T_1 was determined by means of the inversion recovery sequence. As shown in Fig. 7, the data can be fitted by a biexponential function, which gives two T_1 times (Table S3†). Notably, the slow relaxation time $T_{1,S}$ is in the same order of magnitude as ac susceptibility measurement (1.8 ms at 5000 Oe and 7 K). This demonstrates that the slow relaxation observed for **2Y** is due to the unpaired electron on the radical bridge. Furthermore, the coherence time T_M can also be detected by means of the Hahn echo sequence (Fig. S18 and Table S3†). The fit to a biexponential function revealed a slow decoherence time constant of 9 ± 2 μs, demonstrating that **2Y** is also a molecular quantum bit.

Ab initio calculations

In order to determine the electronic structures experimentally and establish the relaxation mechanism, we attempted to perform optical studies (MCD and luminescence), but no usable data was obtained due to the $CA^{2-}/CA^{3-\bullet}$ absorption in the

visible region precluding investigations of f–f transitions (Fig. S3†).[43,44] Therefore, multi-reference *ab initio* calculations (LDF-CAHF + CASCI/SI-SO, detailed information in ESI†)[45] were performed, which gave important information on local ground and excited states of **1Dy** and **1Tb**.[46,47] The g_z values of ground doublet states are indicative of easy-axis anisotropy for **1Dy** (19.76) and **1Tb** (17.26), approaching values expected for a $m_J = \pm 15/2$ and ± 6 ground state, respectively. The local easy axes point toward the CA^{2-} ligand (Fig. S19†), which exhibits shorter bond distances *i.e.* stronger crystal field interactions to lanthanide centers than $HBpz_3^-$ ligands. The angle between the g_z orientation and the vector connecting two lanthanide centers is smaller in **1Dy** (9°) than **1Tb** (31°). More importantly, non-negligible transverse components of the *g*-tensor ($g_x = 0.029$, $g_y = 0.036$) are found in the ground Kramers doublet of **1Dy**, which leads to the strong quantum tunneling of magnetization as a result of mixed microstates (Table S4†). As a non-Kramers ion, the ground pseudo-doublet of **1Tb** can be split in a low-symmetry crystal field and we find a large intrinsic tunneling gap of 2.5 cm^{-1} (Table S5†). This is consistent with the absence of SMM behavior in zero field for **1Tb**. Furthermore, the total splitting for the ground multiplets of the Dy^{III} and Tb^{III} ions is below 500 cm^{-1}, indicating a weak crystal field environment. For **1Dy** the first excited doublet is on 84 cm^{-1} (120 K), which is much higher than U_{eff} from ac susceptibility measurements suggesting the inefficiency of Orbach process here. The large size of the magnetic cores and the absence of molecular structures preclude *ab initio* calculations of complexes **2Ln**. Instead we obtain the effective information of ground states *via* electron paramagnetic resonance (HF-EPR) spectroscopy.

Multifrequency high-field electron paramagnetic resonance (HF-EPR) spectroscopy

EPR proved to be a powerful method to detect the geometric and electronic structures of paramagnetic systems,[48] but it is rarely applied in lanthanide systems due to their EPR-silence or weak signals.[36,49,50] An exception is the spin-only Gd^{III} ion with half-filled f-shell, which gives well resolved EPR signals, thus providing rich information on the crystal field environment.[51] Measuring EPR spectra at high fields and frequencies often simplifies the analysis because the Zeeman term becomes dominant in the spin Hamiltonian.[52] Here we mainly focus on the investigations on Gd compounds from diluted sample **Gd@1Y** to the undiluted sample **1Gd** and then the reduced sample **2Gd**, which provides detailed information on the local crystal field of lanthanide center and exchange coupling interaction between them. Notably, this is the first time that the exchange coupling in a radical-bridged dinuclear lanthanide system is investigated in detail by means of HFEPR.

Fig. S20† shows the temperature-dependence of HF-EPR spectra collected at 320 GHz for diluted sample **Gd@1Y**. Here the parallel transitions appear at low field and the spectral weight increases towards low field on decreasing temperature, which corresponds to a negative zero field splitting parameter *D*. Furthermore, the high field perpendicular transitions reveal small splittings, typical of rhombic distortion. Therefore, a suitable spin Hamiltonian is $\mathscr{H}_{Gd} = \mu_B \hat{S}\cdot g\cdot \hat{H} + D\hat{S}_z^2 + E(\hat{S}_x^2 - \hat{S}_y^2)$. Best simulation parameters are $D = -0.13$ cm^{-1}, $E = 0.014$ cm^{-1} and $g_{xx} = 1.991$, $g_{yy} = 1.987$, $g_{zz} = 1.986$ (Fig. 8). Similar values were reported in a preliminary study in literature.[11] When compared with the mononuclear compound $Gd(HBpz_3)_2(Trp)$ (Trp = 2-hydroxy-2,4,6-cycloheptantrienone, $D = -0.123$ cm^{-1}, $E/D = 0.22$),[14,53] the magnitude of *D* value is comparable, while *E*/*D* is much smaller. This suggests that the axiality of the crystal field is improved when substituting the Trp with a CA ligand. However, the high *E*/*D* value is indicative of a large transversal component in such a crystal field environment, and may further explain the modest SMM behaviour of **1Dy**.

In contrast, the HFEPR spectra of undiluted **1Gd** exhibit further splitting of the resonance lines arising from the weak magnetic interaction between Gd centers, as is shown in Fig. 9 and S21.† A Hamiltonian that includes all relevant terms is $\mathscr{H} = \mathscr{H}_{Gd1} + \mathscr{H}_{Gd2} + J\hat{S}_{Gd1}\cdot\hat{S}_{Gd2}$, where the single ion Hamiltonians are strictly equal due to the inversion symmetry of the complexes. On the basis of this Hamiltonian, good simulations of the experimental spectra at different frequencies were obtained for $J = 0.009$ cm^{-1}, and the same single ion parameters as for the dilute compound. Such a weak interaction cannot be easily determined from bulk magnetic measurements (Fig. 5).[49,54] Naturally, more complicated spectra are observed in the reduced Gd compound **2Gd**, which are clearly distinct from those recorded **1Gd** (Fig. S22†). The absence of resonance lines attributable to **1Gd** underlines the purity of **2Gd**. The temperature dependent spectra at 290 GHz (Fig. S22†) reveal a fine structure progression and increasing weight towards low field on decreasing temperature, suggesting the presence of zero field splitting. Using the Hamiltonian $\mathscr{H} = J\hat{S}_{rad}(\hat{S}_{Gd1} + \hat{S}_{Gd2}) + \mu_B\hat{S}\cdot g\cdot\hat{H} + \sum D\hat{S}_z^2$ for simulations (Fig. 9 and S23†) gave the following parameters: $g_{rad} = g_{Gd} = 1.976$, $J = 3.1$ cm^{-1}, $D_{Gd} = -0.11$ cm^{-1}. Inclusion of a rhombic zero-field splitting term did not improve results. The values are reasonable when compared with the above results, and they give good simulations of the temperature-dependent $\chi_M T$ values and low-temperature magnetization (Fig. S10 and S24†). Therefore, we consider

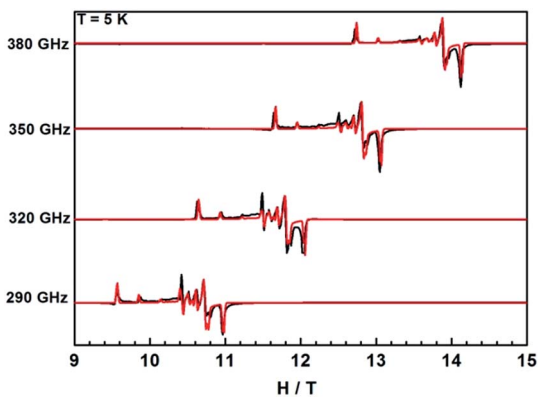

Fig. 8 HFEPR spectra of sample **Gd@1Y** recorded at 5 K and various frequencies. The black lines illustrate the experimental spectra while red lines correspond to simulations using a suitable spin Hamiltonian (see text).

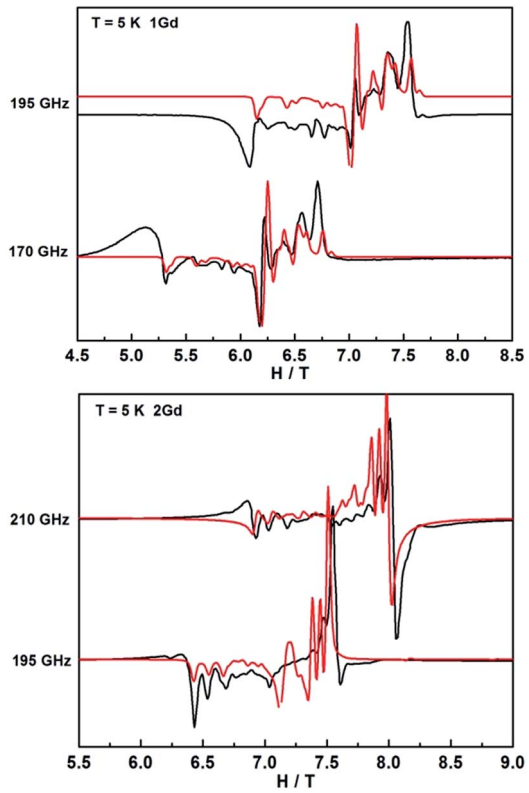

Fig. 9 HFEPR spectra of **1Gd** and **2Gd** recorded at 5 K and various frequencies. The red lines correspond to simulations using the spin Hamiltonian reported in the text.

these parameters to be more reliable than those obtained from magnetic measurements alone.

For **1Dy**, no EPR was observed, due to the strong axiality of the ground Kramers doublet leading to the intra-ground doublet transition being strongly forbidden. This is in agreement with literature reports.[11] In contrast, HFEPR measurements on a powder sample of **1Tb** revealed a weak but clear resonance line with large effective *g*-value (Fig. S25†). A linear fit of field–frequency plot gave a *g*-value of 16.1 indicative of a highly axial ground state, where the *g*-value found is only slightly smaller than that calculated (see above). Extrapolation of the field–frequency plot gave a zero field resonance frequency of 46 GHz (1.5 cm^{-1}), in good agreement with *ab initio* calculations. Interestingly, clear HFEPR spectra could also be obtained for **2Tb** (Fig. 10), which are to the best of our knowledge the first EPR spectra recorded for terbium–radical complexes. These spectra display four distinct features. The strongest resonance line (I in Fig. 10) has an effective *g*-value of 2.06 ± 0.02 and a zero energy gap at zero field. Such a resonance line was not observed for **1Tb** and must therefore attributed to the radical species. The significant difference of the *g*-value from that of the free electron reveals the participation of the terbium ion in the orbital carrying the unpaired electron. Second, a resonance line (II) with large effective *g*-value (11.8 ± 0.8) and a sizable zero field gap of 72 ± 17 GHz (2.35 cm^{-1}) is observed, which we attribute to the intra-pseudo-doublet transition. The different zero-field gap and *g*-values reveal the influence of the

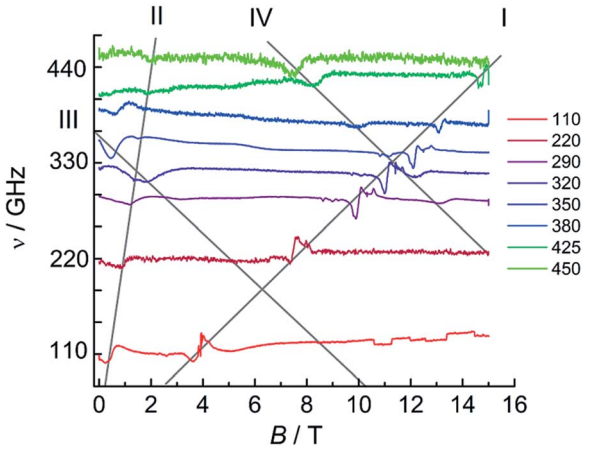

Fig. 10 HFEPR spectra of **2Tb** recorded at 5 K and various frequencies. The grey lines are guides to the eye.

reduction of the bridging ligand on the terbium crystal field splitting. Finally, two weaker resonance lines are observed (III, IV) with decreasing resonance fields with increasing microwave frequencies and finite zero-field gaps of 12 and 22 cm^{-1} respectively. We attribute these finite gaps to the exchange splittings of the energy levels resulting from the presence of a radical bridge. A more quantitative analysis would require consideration of the full exchange coupled system, employing a suitable Hamiltonian featuring exchange coupling, crystal field and Zeeman terms. Unfortunately, the amount of data available precludes such an analysis. Note that we cannot approximate the lanthanide ions by effective $S = 1/2$ spins, due to the non-Kramers nature of terbium(III). Also, the exchange couplings are typically highly anisotropic.[49] Furthermore, we have no information on the energetic position of the excited pseudo-doublets of the terbium ions, and cannot calculate these. Finally, in the absence of structural data, we cannot assume there to be an inversion center between the two terbium centers, which may therefore be inequivalent. A simplified fit employing two $S = 1$ effective spins with very large D values to simulate the ground pseudo doublets of the terbium ions did reproduce some of the salient features of the spectra, notably the strong resonance line I (Fig. S26†). Here, we used the same Hamiltonian as for **2Gd**, $\mathscr{H} = J\hat{S}_{rad}(\hat{S}_1 + \hat{S}_2) + \mu_B\hat{S}\cdot g\cdot\hat{H} + \sum D\hat{S}_z{}^2$, with $S_{rad} = 1/2$, $S_1 = S_2 = 1$, $D = -2000$ cm^{-1}, $E = 1$ cm^{-1}, $g_{rad} = 2.07$, $g_{Tb} = (0.1, 0.1, 4.0)$, $J = 4.3$ cm^{-1}.

Conclusions

We have presented an in-depth study of tetraoxolene bridged dinuclear lanthanide complexes. Successful chemical reduction of the bridging ligand gives rise to strongly coupled radical-bridged systems with improved SMM properties. HFEPR measurements elucidated the magnetic coupling in these systems. The modest SMM behavior is most likely due to limited axiality of the local crystal field which may be improved by using Cp rather than $HBpz_3^-$ as ancillary ligands and we are currently pursuing the synthetic work involved in this direction.

Experimental section

The chemical reductions described below were performed under nitrogen with rigorous exclusion of air and water using Schlenk, vacuum line, and glovebox techniques. Solvents were dried with sodium benzophenone ketyl or CaH_2 under pure argon atmosphere prior to use. Cobaltocene was purchased from Alfa Aesar and used as received. Elemental analyses were performed in a Perkin Elmer CHSN/O Analyzer. IR spectra were recorded on Bruker ALPHA-T spectrometer with KBr pellets. UV-vis spectra were recorded on Perkin Elmer UV/Vis Spectrometer in CH_3CN solution. The ESI mass spectra were recorded on Bruker microTOF-Q ESI-MS with the non-radical and radical compounds in positive and negative modes, respectively. Cyclic voltammograms were recorded with a three electrode setup (glassy carbon working electrode, Pt counter electrode, Ag/AgCl reference electrode) using a Metrohm Autolab potentiostat. The potentials are referenced against an internal ferrocene/ferrocenium redox couple. Spectroelectrochemical measurements were carried out using an optically transparent thin layer electrochemical (OTTLE) cell.[55]

$[(HBpz_3)_2Ln(\mu\text{-}CA)Ln(HBpz_3)_2]\cdot 2CH_2Cl_2$ (1Ln)

A solution of K_2CA was prepared by the reaction of H_2CA (0.105 g, 0.5 mmol) and KOH in 10 ml H_2O. It was added to a stirred aqueous solution (20 ml) of lanthanide chloride hydrate (1 mmol) as well as an aqueous solution (10 ml) of $K(HBpz_3)$ (0.5 g, 2 mmol). The solution was stirred for 15 min. The resulting purple precipitate was filtered off, washed three times with water, and dried under vacuum. The crude product was recrystallized from dichloromethane/acetonitrile several times (yield = 40%). Single crystals, suitable for X-ray diffraction analysis, were obtained by slow evaporation of the solvent in dichloromethane–acetonitrile solution. Elemental analysis (%) results are listed in Table S6.† Mass and infrared spectra were discussed above.

Synthesis of diluted sample Gd@1Y

The procedure was the same as that used for the above except that accurately measured 50 : 1 molar ratios of yttrium(III) and gadolinium(III) chloride was used as rare-earth salt.

$[(HBpz_3)_2Ln(\mu\text{-}CA^{\bullet})Ln(HBpz_3)_2]^{-}\cdot[CoCp_2]^{+}$ (2Ln)

Compounds **1Ln** were dried under vacuum before being transferred into the glovebox. A sample (0.1 mmol) of **1Ln** was dissolved in tetrahydrofuran (20 ml), to which a tetrahydrofuran solution of cobaltocene (0.1 mmol, 10 ml) was added slowly. Immediately, a green precipitate was obtained. The reaction mixture was stirred for another two hours. The precipitate was filtered off, washed several times with tetrahydrofuran, and dried under vacuum. Elemental analysis results are listed in Table S6.† Mass and infrared spectra were discussed above.

X-ray data collection and structure determinations

Crystallographic data of complexes **1Dy**, **1Tb** and **1Y** were collected on a Bruker Kappa APEXII Duo diffractometer with a monochromatic Mo-Kα radiation ($\lambda = 0.71073$ Å) at 156 (2) K. For complex **1Gd**, the data was collected on STOE IPDS II diffractometer equipped with Mo-Kα radiation, a nickel filter and an image plate detector at room temperature. The structures were solved by direct methods and refined on F^2 by full-matrix least squares by means of SHELXS-2013 and SHELXL-2013 programs.[56] The location of lanthanide atoms was easily determined, and B, Cl, O, N and C atoms were subsequently determined from the difference Fourier maps. All non-hydrogen atoms were refined with anisotropic thermal parameters. The H atoms were introduced in calculated positions and refined with fixed geometry with respect to their carrier atoms. CCDC-1568172 (**1Dy**), 1568173 (**1Tb**), 1568174 (**1Gd**), 1568175 (**1Y**).† The **1Dy** and **1Y** were also reported recently by Boskovic *et al.*[11]

Magnetic measurements

Magnetic susceptibility measurements were carried out using a Quantum Design MPMS3 SQUID magnetometer equipped with a 7 T magnet. The direct current (dc) measurements were performed with an external magnetic field of 1000 Oe in the temperature range 1.8–300 K, and the alternating-current (ac) measurements were measured in a 3.0 Oe ac field oscillating at different frequencies from 0.1 to 1000 Hz. The experimental magnetic susceptibility data are corrected for the diamagnetism estimated from Pascal's tables[57] and sample holder calibration.

EPR measurements

High-frequency EPR (HFEPR) spectra at 5 K and frequencies between 110 and 450 GHz were recorded on a home-built spectrometer featuring an VDI signal generator, a VDI amplifier-multiplier chain, a Thomas Keating quasi-optical bridge, an Oxford Instruments 15/17 T solenoid cryomagnet and a QMC Instruments InSb hot electron bolometer. The sample was studied as pressed Teflon-wrapped powder pellets. EPR spectra were simulated using the Easyspin program.[58] All pulsed measurements were performed on a homebuilt Q-band EPR spectrometer,[59] where an Oxford Instruments CF935 continuous flow helium cryostat was used. The sample was dissolved in acetonitrile (1 mM), filled in quartz tubes, degassed by three freeze–pump–thaw cycles followed by flame sealing. Relaxation measurements were performed at the field position of the most intense resonance line. Spin–lattice relaxation times were measured by inversion recovery, phase memory times *via* Hahn echo pulse sequences; both were fitted with exponential functions.

Author contributions

J. v. S. designed and supervised the research; P. Z. synthesized and characterized the complexes; W. F. performed the crystallographic investigation; M. K., M. P. and P. Z. performed the magnetometric and HF-EPR measurements and analyses; P. P. H. and L. U. performed the *ab initio* calculations under the

supervision of H. S. and G. R.; S. L. performed and analyzed the Q-band pulsed EPR measurements; M. R. R. performed the electrochemical experiments; P. Z. and J. v. S. wrote the manuscript with input from all authors.

Conflicts of interest

There are no conflicts to declare.

Acknowledgements

We acknowledge funding from DFG (SL104/5-1, SPP1601), the Alexander von Humboldt Foundation (postdoctoral fellowship for P. Z.), the Vector foundation, the Foundation of the Federal State of Baden-Württemberg (PhD fellowship to P. P. H.), the Zeiss Foundation (PhD fellowship for S. L.). We thank Ms Luzia S. Germann and Robert E. Dinnebier for assistance in X-ray data collection (**1Gd**) and Dr Petr Neugebauer for experimental help in the HFEPR measurements.

Notes and references

1 B. Sarkar, D. Schweinfurth, N. Deibel and F. Weisser, *Coord. Chem. Rev.*, 2015, **293**, 250–262.
2 J. S. Miller and K. S. Min, *Angew. Chem., Int. Ed.*, 2009, **48**, 262–272.
3 M. L. Mercuri, F. Congiu, G. Concas and S. A. Sahadevan, *Magnetochemistry*, 2017, **3**, 17.
4 A. Dei, D. Gatteschi, C. Sangregorio and L. Sorace, *Acc. Chem. Res.*, 2004, **37**, 827–835.
5 C. Carbonera, A. Dei, J.-F. Létard, C. Sangregorio and L. Sorace, *Angew. Chem., Int. Ed.*, 2004, **43**, 3136–3138.
6 K. S. Min, A. G. DiPasquale, J. A. Golen, A. L. Rheingold and J. S. Miller, *J. Am. Chem. Soc.*, 2007, **129**, 2360–2368.
7 D. Schweinfurth, Y. Rechkemmer, S. Hohloch, N. Deibel, I. Peremykin, J. Fiedler, R. Marx, P. Neugebauer, J. van Slageren and B. Sarkar, *Chem.–Eur. J.*, 2014, **20**, 3475–3486.
8 I.-R. Jeon, J. G. Park, D. J. Xiao and T. D. Harris, *J. Am. Chem. Soc.*, 2013, **135**, 16845–16848.
9 S. Demir, I.-R. Jeon, J. R. Long and T. D. Harris, *Coord. Chem. Rev.*, 2015, **289**, 149–176.
10 A. Dei, D. Gatteschi, C. A. Massa, L. A. Pardi, S. Poussereau and L. Sorace, *Chem.–Eur. J.*, 2000, **6**, 4580–4586.
11 M. A. Dunstan, E. Rousset, M.-E. Boulon, R. W. Gable, L. Sorace and C. Boskovic, *Dalton Trans.*, 2017, **46**, 13756–13767.
12 J. O. Moilanen, A. Mansikkamaki, M. Lahtinen, F.-S. Guo, E. Kalenius, R. A. Layfield and L. F. Chibotaru, *Dalton Trans.*, 2017, **46**, 13582–13589.
13 A. Caneschi, A. Dei, D. Gatteschi, L. Sorace and K. Vostrikova, *Angew. Chem., Int. Ed.*, 2000, **39**, 246–248.
14 A. Caneschi, A. Dei, D. Gatteschi, C. A. Massa, L. A. Pardi, S. Poussereau and L. Sorace, *Chem. Phys. Lett.*, 2003, **371**, 694–699.
15 N. Claiser, M. Souhassou, C. Lecomte, B. Gillon, C. Carbonera, A. Caneschi, A. Dei, D. Gatteschi, A. Bencini, Y. Pontillon and E. Lelièvre-Berna, *J. Phys. Chem. B*, 2005, **109**, 2723–2732.
16 S. T. Liddle and J. van Slageren, *Chem. Soc. Rev.*, 2015, **44**, 6655–6669.
17 J. D. Rinehart, M. Fang, W. J. Evans and J. R. Long, *Nat. Chem.*, 2011, **3**, 538–542.
18 J. D. Rinehart, M. Fang, W. J. Evans and J. R. Long, *J. Am. Chem. Soc.*, 2011, **133**, 14236–14239.
19 P. Zhang, Y.-N. Guo and J. Tang, *Coord. Chem. Rev.*, 2013, **257**, 1728–1763.
20 F. Habib and M. Murugesu, *Chem. Soc. Rev.*, 2013, **42**, 3278–3288.
21 S. Demir, J. M. Zadrozny, M. Nippe and J. R. Long, *J. Am. Chem. Soc.*, 2012, **134**, 18546–18549.
22 S. Demir, M. Nippe, M. I. Gonzalez and J. R. Long, *Chem. Sci.*, 2014, **5**, 4701–4711.
23 B. S. Dolinar, S. Gomez-Coca, D. I. Alexandropoulos and K. R. Dunbar, *Chem. Commun.*, 2017, **53**, 2283–2286.
24 C. A. Gould, L. E. Darago, M. I. Gonzalez, S. Demir and J. R. Long, *Angew. Chem., Int. Ed.*, 2017, **56**, 10103–10107.
25 F.-S. Guo and R. A. Layfield, *Chem. Commun.*, 2017, **53**, 3130–3133.
26 G. F. Xu, Q. L. Wang, P. Gamez, Y. Ma, R. Clérac, J. K. Tang, S. P. Yan, P. Cheng and D. Z. Liao, *Chem. Commun.*, 2010, **46**, 1506–1508.
27 N. G. Connelly and W. E. Geiger, *Chem. Rev.*, 1996, **96**, 877–910.
28 T. P. Gerasimova and S. A. Katsyuba, *J. Organomet. Chem.*, 2015, **776**, 30–34.
29 M. Martínez-Pérez, S. Cardona-Serra, C. Schlegel, F. Moro, P. Alonso, H. Prima-García, J. Clemente-Juan, M. Evangelisti, A. Gaita-Ariño, J. Sesé, J. van Slageren, E. Coronado and F. Luis, *Phys. Rev. Lett.*, 2012, **108**, 247213.
30 M. Benmelouka, J. Van Tol, A. Borel, M. Port, L. Helm, L. C. Brunel and A. E. Merbach, *J. Am. Chem. Soc.*, 2006, **128**, 7807–7816.
31 E. Lucaccini, J. J. Baldoví, L. Chelazzi, A.-L. Barra, F. Grepioni, J.-P. Costes and L. Sorace, *Inorg. Chem.*, 2017, **56**, 4728–4738.
32 P.-E. Car, M. Perfetti, M. Mannini, A. Favre, A. Caneschi and R. Sessoli, *Chem. Commun.*, 2011, **47**, 3751–3753.
33 S. A. Sulway, R. A. Layfield, F. Tuna, W. Wernsdorfer and R. E. P. Winpenny, *Chem. Commun.*, 2012, **48**, 1508–1510.
34 J. D. Rinehart, K. R. Meihaus and J. R. Long, *J. Am. Chem. Soc.*, 2010, **132**, 7572–7573.
35 S. D. Jiang, B. W. Wang, G. Su, Z. M. Wang and S. Gao, *Angew. Chem., Int. Ed.*, 2010, **49**, 7448–7451.
36 E. Lucaccini, L. Sorace, M. Perfetti, J.-P. Costes and R. Sessoli, *Chem. Commun.*, 2014, **50**, 1648–1651.
37 J.-L. Liu, K. Yuan, J.-D. Leng, L. Ungur, W. Wernsdorfer, F.-S. Guo, L. F. Chibotaru and M.-L. Tong, *Inorg. Chem.*, 2012, **51**, 8538–8544.
38 L. Zhang, Y.-Q. Zhang, P. Zhang, L. Zhao, M. Guo and J. Tang, *Inorg. Chem.*, 2017, **56**, 7882–7889.
39 A. Lunghi, F. Totti, R. Sessoli and S. Sanvito, *Nat. Commun.*, 2017, **8**, 14620.
40 K. R. Meihaus, S. G. Minasian, W. W. Lukens, S. A. Kozimor, D. K. Shuh, T. Tyliszczak and J. R. Long, *J. Am. Chem. Soc.*, 2014, **136**, 6056–6068.

41 K. R. Meihaus, J. D. Rinehart and J. R. Long, *Inorg. Chem.*, 2011, **50**, 8484–8489.
42 K. Bader, D. Dengler, S. Lenz, B. Endeward, S.-D. Jiang, P. Neugebauer and J. van Slageren, *Nat. Commun.*, 2014, **5**, 5304.
43 M. Abdus Subhan, R. Kawahata, H. Nakata, A. Fuyuhiro, T. Tsukuda and S. Kaizaki, *Inorg. Chim. Acta*, 2004, **357**, 3139–3146.
44 Y. Rechkemmer, J. E. Fischer, R. Marx, M. Dörfel, P. Neugebauer, S. Horvath, M. Gysler, T. Brock-Nannestad, W. Frey, M. F. Reid and J. van Slageren, *J. Am. Chem. Soc.*, 2015, **137**, 13114–13120.
45 P. P. Hallmen, C. Köppl, G. Rauhut, H. Stoll and J. v. Slageren, *J. Chem. Phys.*, 2017, **147**, 164101.
46 C. Köppl and H.-J. Werner, *J. Chem. Theory Comput.*, 2016, **12**, 3122–3134.
47 L. F. Chibotaru and L. Ungur, *J. Chem. Phys.*, 2012, **137**, 064112–064122.
48 C. Duboc, *Chem. Soc. Rev.*, 2016, **45**, 5834–5847.
49 E. Moreno Pineda, N. F. Chilton, R. Marx, M. Dörfel, D. O. Sells, P. Neugebauer, S.-D. Jiang, D. Collison, J. van Slageren, E. J. L. McInnes and R. E. P. Winpenny, *Nat. Commun.*, 2014, **5**, 5243.
50 M. Gysler, F. El Hallak, L. Ungur, R. Marx, M. Hakl, P. Neugebauer, Y. Rechkemmer, Y. Lan, I. Sheikin, M. Orlita, C. E. Anson, A. K. Powell, R. Sessoli, L. F. Chibotaru and J. van Slageren, *Chem. Sci.*, 2016, **7**, 4347–4354.
51 C. Benelli and D. Gatteschi, in *Introduction to Molecular Magnetism*, Wiley-VCH Verlag GmbH & Co. KGaA, 2015, pp. 375–393.
52 J. Krzystek, A. Ozarowski and J. Telser, *Coord. Chem. Rev.*, 2006, **250**, 2308–2324.
53 A. Caneschi, A. Dei, D. Gatteschi, S. Poussereau and L. Sorace, *Dalton Trans.*, 2004, 1048–1055.
54 A. Dalaloyan, M. Qi, S. Ruthstein, S. Vega, A. Godt, A. Feintuch and D. Goldfarb, *Phys. Chem. Chem. Phys.*, 2015, **17**, 18464–18476.
55 W. Kaim and J. Fiedler, *Chem. Soc. Rev.*, 2009, **38**, 3373–3382.
56 G. M. Sheldrick, *Acta Crystallogr., Sect. A: Found. Crystallogr.*, 2008, **64**, 112.
57 E. A. Boudreaux and L. N. Mulay, *Theory and Applications of Molecular Paramagnetism*, John Wiley & Sons, New York, 1976.
58 S. Stoll and A. Schweiger, *J. Magn. Reson.*, 2006, **178**, 42–55.
59 I. Tkach, A. Baldansuren, E. Kalabukhova, S. Lukin, A. Sitnikov, A. Tsvir, M. Ischenko, Y. Rosentzweig and E. Roduner, *Appl. Magn. Reson.*, 2008, **35**, 95–112.